Unraveling Internal Structures of Highly Luminescent PbSe Nanocrystallites Using Variable-Energy Synchrotron Radiation Photoelectron Spectroscopy

Sameer Sapra,[†] J. Nanda,[‡,§] Jeffrey M. Pietryga,[‡] Jennifer A. Hollingsworth,[‡] and D. D. Sarma*[,†]

Solid State and Structural Chemistry Unit, Indian Institute of Science, Bangalore 560012, India, and C-PCS, Los Alamos National Laboratory, Los Alamos, New Mexico 87545

Received: March 27, 2006; In Final Form: June 6, 2006

The internal structure of PbSe nanocrystals was deduced using synchrotron X-ray photoemission spectroscopy for three different sizes of nanocrystals. The photoemission data revealed the layered structure of PbSe nanocrystals with the crystalline PbSe core surrounded by a nonstoichiometric $Pb_{1-x}Se$ shell, finally passivated by a capping agent in the outermost layer. A detailed analysis of the experimental data yielded quantitative information on the thickness of three different layers, which is unavailable through any other technique; moreover, the overall sizes of the nanocrystals probed by transmission electron microscopy were in agreement with the corresponding quantity obtained in the present experiment. The present results provide a plausible explanation for the strong variation in the photoluminescence intensity with size observed for these nanocrystals.

In recent years, a number of colloidal synthetic routes have been successfully developed for producing size-monodispersed nanocrystallites (NCs), leading to NCs of predetermined shape, size, and functionality.[1−4] However, the surfaces and interfaces of these materials are largely determined by the intricacies of the synthetic route such as temperature, reactant precursors, solvents, and, more importantly, the passivation material. Changing one or more of these synthetic parameters affects the growth dynamics, thereby leading to NCs with different surface structures and composition.[5−8] Such changes are, however, accompanied by drastically different properties such as quantum efficiencies of fluorescence and surface functionalities.[9−11] Surfaces and interfaces also play a vital role in determining the thermodynamical stability of nanoparticles. Therefore, understanding the correlation between the surface/interfacial properties of such nanoscale materials and their associated perturbations of the electronic properties is the key toward integrating such materials for real device applications. There have been a few reports in the literature related to the study of surfaces and interfaces using NMR,[12,13] X-ray absorption near-edge spectroscopy (XANES),[14] and X-ray photoelectron spectroscopy (XPS).[15−19]

PbSe in the bulk form is a direct gap semiconductor having a band gap of 0.26 eV at 300 K, which has application as an IR gain medium in quantum well devices.[20] Recently, there has been great interest in the study of PbSe NCs because of their strong quantum size effects leading to a continuous range of emissions from near-infrared to mid-infrared wavelengths.[2,21] Recent advances in colloidal synthesis have led to the synthesis of monodisperse PbSe NCs with emission yields as high as 70% in smaller NCs.[22] This has already opened up a few potential applications as efficient emitters in telecommunication windows compared to organic dyes, which are poor performers in terms of their photostability and photoluminescence (PL) efficiency. A recent demonstration of optical gain and amplified spontaneous emission in PbSe NCs[23] provides further opportunities for their application as tunable infrared lasers and waveguides. However, there still remains the issue of quantum yield of the NCs vis-à-vis their sizes, as reported in a previous article.[22] For example, for a 3 nm diameter PbSe NC emitting at 1.03 eV, the PL efficiency is close to 70%, while the corresponding values for a 12 nm NC emitting at 0.44 eV is a mere 4%. This observation of larger quantum efficiency for a smaller dot appears somewhat counter-intuitive, since a larger proportion of surface atoms and therefore a greater abundance of surface states in the smaller NCs are expected to quench the PL more efficiently, thereby reducing the quantum yield compared to that of larger NCs. The contrasting experimental observation suggests that either a systematic increase in the oscillator strength with a decrease in the NC size dominates or the surfaces of the NCs play a nontrivial and unexpected role in determining the eventual PL efficiency.

In this article, we report an XPS investigation on three different sizes of PbSe NCs synthesized using the chemical route.[22] Using the tunability of the photon energies at a synchrotron source, we could vary the surface sensitivity of this technique to probe the spatial variations and inhomogeneities of atomic compositions, in terms of their chemical bonding and coordination, as we move from the core to the surface of the nanocrystallite. The photoelectron signal originating from a particular atom is sensitive to its chemical environment, which is reflected as a shift in the binding energy. Thus, within resolution limits, spectral decomposition of the photoelectron core-level signal can yield valuable chemical information pertaining to the NCs. We investigate different sizes of PbSe NCs to monitor the relative variation of surface to bulk photoelectron signals directly, giving us a semiquantitative idea about their surface composition and stability without the need for any detailed analysis. Briefly, our studies revealed two chemically distinct sites for Pb, corresponding to the Pb atoms in the core of the nanocrystallite and another chemically distinct

* Corresponding author. E-mail: sarma@sscu.iisc.ernet.in. Fax: +91 80 2360 1310.
[†] Indian Institute of Science.
[‡] Los Alamos National Laboratory.
[§] Present Address: Research and Innovation Center, Ford Motor Company, Dearborn, MI 48121.

10.1021/jp061885p CCC: $33.50
Published on Web 07/14/2006

species of Pb residing at the surface region. Interestingly, we could resolve three distinct chemical sites for Se;[24] these could be attributed to Se at the core, the Se at the surface of the NCs, and the Se that is a part of the capping material, namely, trioctylphosphine selenium (TOPSe). We also noticed an additional Se component (total of four Se species) in the case of the larger, 11 nm diameter NCs arising from oxide islands; our experiments suggest that these exist as separate entities, presumably from the oxidation of some free Se and not part of the NCs internal structure. On the basis of a detailed analysis of various XPS signal intensities originating from each individual species of the nanocrystallite, we could reconstruct the internal structure of the nanocrystallite in great detail, obtaining the individual thicknesses of various layers defining the NC. We show that such detailed understanding, only possible using a tunable synchrotron source, also provides us with a possible explanation for the surprisingly poor PL yield for larger PbSe NCs.

Experimental Section

Synthesis of PbSe NCs. PbSe NCs of different sizes used for spectroscopic study were synthesized using chemical routes published in the literature.[21,22] Briefly, the NCs were synthesized by the reaction of lead acetate trihydrate and TOPSe in the presence of oleic acid and trioctylphosphine in hot ($\geq$200 °C) phenyl ether under inert atmosphere. The product nanocrystals are then precipitated by the addition of methanol, collected by centrifugation, and redispersed in hexane. Excess ligand was removed by repeating the precipitation, centrifugation, and redispersal steps. No further size-selective procedures were carried out on any sample.

Structural and Optical Characterization. The synthesized NCs were characterized using transmission electron microscopy (TEM) and X-ray diffraction (XRD). The TEM measurements were performed using a JEOL-300 microscope with a magnification voltage of 300 keV. The samples for microscopy were prepared by dispersing the diluted NC sample in hexane on carbon-coated copper grids. XRD was performed using a Philips D-500 diffractometer at an operating anode voltage of 35 keV and a current of 35 A.

The PL spectra for diluted NC samples in hexane or chloroform solution were recorded with a cooled InSb detector at an excitation wavelength of 808 nm. The quantum efficiencies were calculated with respect to IR26, and corrections were made to account for the grating and detector efficiencies.

Synchrotron XPS Studies. Photoemission spectroscopy was performed on three sizes of PbSe NCs using the synchrotron radiation source Elettra (Trieste, Italy) at the vacuum-ultraviolet (VUV) beamline. To probe the surface, as well as the bulk of the NCs with the highest sensitivities for each case, we used a series of photon energies between 800 and 200 eV. The core levels of primary interest in our case were the Pb 4f, Se 3d, and P 2p core levels. The background arising from inelastic scattering of outgoing photoelectrons was removed in each case using the Shirley iterative procedure. Raw spectra without any background subtraction are available as Supporting Information. To avoid charging the samples during the photoemission process, the samples were mixed with graphite powder. The mixture containing graphite and the NCs was then pressed firmly onto an In foil and mounted in the spectrometer. The experiments were carried out at a base pressure of 8×10^{-10} Torr under identical source and detector settings.

Spectral Fitting. The photoemission spectra were decomposed into individual contribution components from distinct chemical species by the least-squared-error fitting procedure. Lorentzian functions, arising from characteristic lifetime broadening, were chosen for each component of the spectra. These functions were then convoluted with a Gaussian function to account for the instrumental resolution. The widths of the two functions were allowed to vary to get the best fit to the experimental spectra. Wherever possible, constraints were imposed on the parameter values, on the basis of physical considerations, thereby restricting the number of freely adjustable parameters in the fitting process. For example, signal intensities from a spin−orbit split pair were constrained to be in the ratio of their degeneracies. Furthermore, the Gaussian function representing the instrumental resolution was fixed for all spectra recorded with the same resolution.

The Lorentzian function is dependent on the lifetime of the hole in the core level. Thus, it is kept the same for different signals from the same core level of an atom. For example, Se 3d core-level spectra were constrained to have the same lifetime broadening, irrespective of whether the Se species belong to the core PbSe, surface-layer $Pb_{1-x}Se$, or as a part of the capping layer. We also note that spectral-fitting is a nonunique process and is susceptible to overinterpretation; for example, the spectral fitting improves monotonically with the number of components used to decompose the total spectrum without any requirement for a physical basis for the existence of such components. Therefore, our approach has been to use the minimum number of components that are absolutely necessary to describe the spectral line shape consistently across all the photon energies used to record any given spectrum.

Results

Photoelectron spectroscopic measurements were carried out on PbSe NCs of three different diameters, namely, 11 ± 0.9, 9 ± 1.0, and 3 ± 0.25 nm. Figure 1 shows the high resolution TEM picture of 11 and 9 nm NCs with clearly resolved lattice fringes. While the 9 nm diameter particles are nearly spherical in shape, the larger 11 nm ones appear to be in transition toward cubic shape, preferring the natural shape of the intrinsic cubic rock-salt structure.[22] XRD (not shown here) reveals the cubic rock-salt phase for all three sizes of PbSe NCs. Normalized PL emission spectra corresponding to the three sizes are shown in Figure 2 with emissions at 1.03, 0.6, and 0.44 eV, respectively. The estimated quantum yield shows a drastic reduction with increasing particle size having values of 4, 25, and 70% for 11, 9, and 3 nm NCs, respectively.

The mean escape depth of the photoemitted electrons depends on their kinetic energy, which can in fact be tuned by changing the incident photon energy.[24] Therefore, by tuning the photon energy available at the synchrotron radiation source, it is possible to selectively probe different depths of the NCs, thereby providing uniquely detailed information on their internal structures. Pb 4f and P 2p spectra were recorded with 800, 600, and 200 eV photon energies, whereas the Se 3d spectra were collected at incident photon energies of 600, 400, and 200 eV. Analyses of each core-level spectra for the three different NC sizes are discussed below.

Pb 4f and P 2p Spectra. The Pb 4f level is spin−orbit split into the $4f_{5/2}$ and $4f_{7/2}$ levels with reported binding energies of 141.7 and 136.9 eV, respectively, in the atomic form. The P 2p levels are close in energy to the Pb 4f levels. P 2p is also split into $J = 3/2$ and $J = 1/2$ components, separated by about 1 eV, due to the spin−orbit coupling. These spectra were recorded for all three NC sizes at 800, 600, and 200 eV, shown in Figure 3 for the small (3a), intermediate (3b), and large (3c) NCs. The

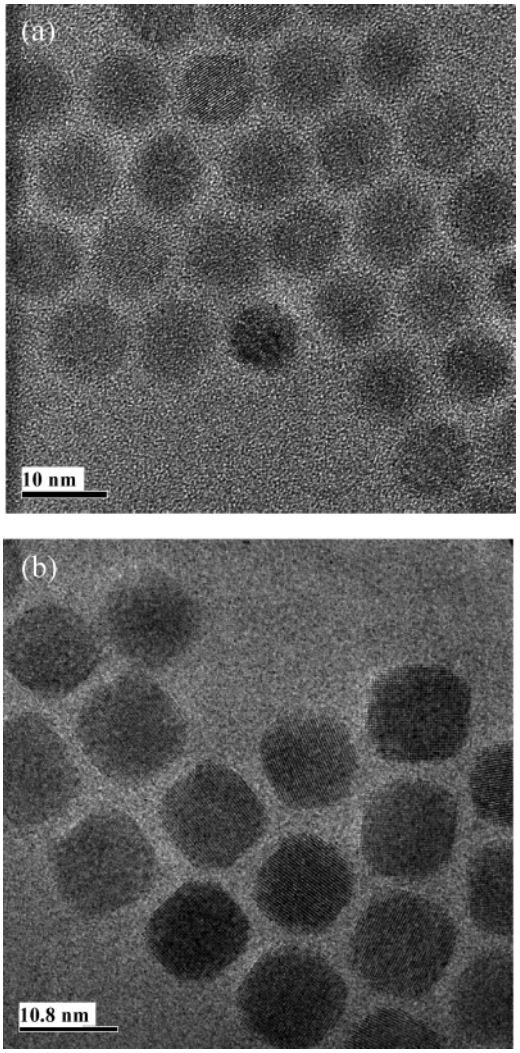

Figure 1. Transmission electron micrographs for (a) 9.0 and (b) 11.0 nm PbSe nanocrystals.

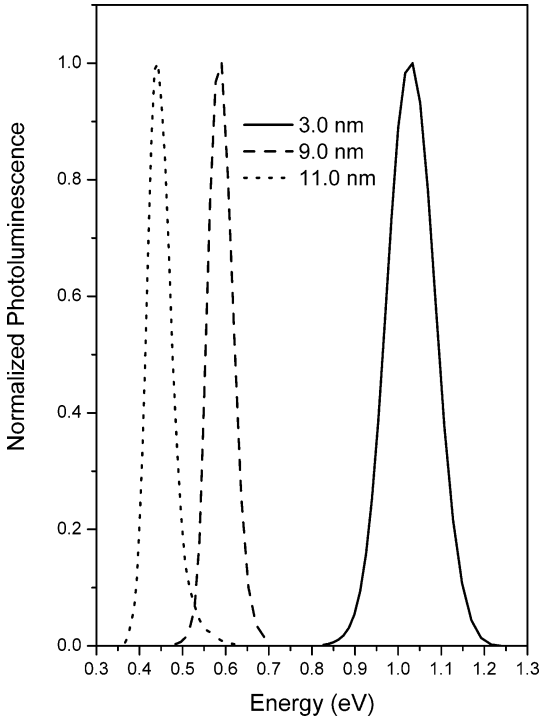

Figure 2. PL spectra for PbSe nanocrystals.

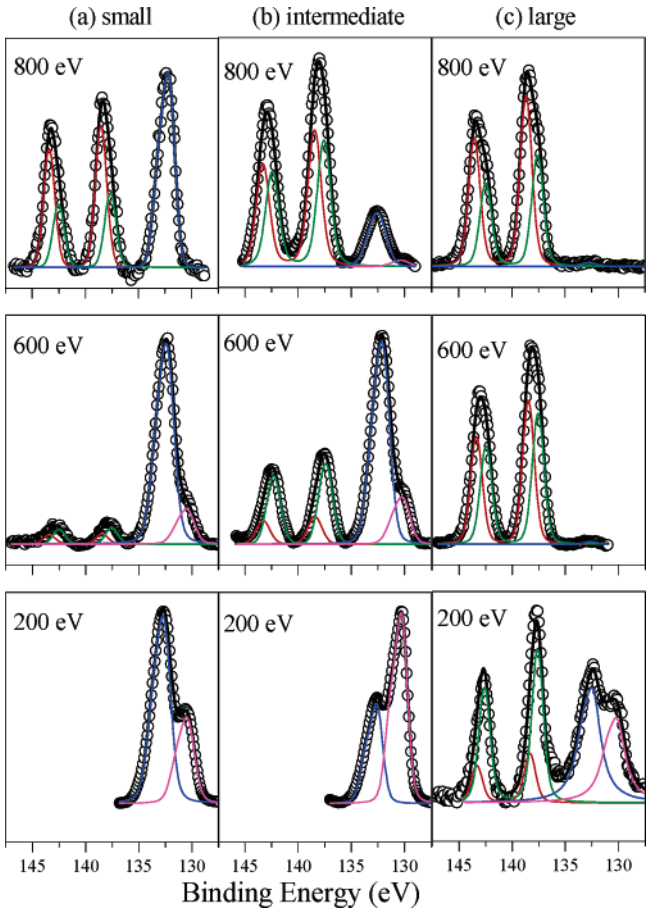

Figure 3. Background-subtracted Pb 4f and P 2p photoemission spectra and fits of (a) small, (b) intermediate sized, and (c) large PbSe nanocrystals.

open circles represent the data points, while various lines are the result of the theoretical analysis discussed before. The features with binding energies less than 135 eV are the P 2p signals. The spin−orbit split doublet feature is not observed for this peak because of the broadening of the $2p_{3/2}$ and the $2p_{1/2}$ components in comparison with the spin−orbit coupling strength. In the spectra recorded with lower photon energies, we observe the presence of two P 2p features, arising from two distinct P species in these samples. The relative intensities of these two features change systematically with a change in the photon energy. The features with binding energies of about 137.5 and 143 eV are from Pb 4f levels. These binding energies are higher than those for atomic Pb due to the positive charge of Pb^{2+} ions. From the data, it is evident that there are at least one species of Pb and two species of P in the system. Thus, we first tried to fit the experimental spectra in terms of a single Pb component and two P species. However, we found that it was not possible to get a reasonable description of the experimental spectra using only one Pb species. At least two Pb species are necessary to get a good fit to the experimental spectra. An analysis for PbS NCs[19] showed that Pb exists in two different sites in the case of PbS too. However, the explanations for the data in the case of PbS and in the present case are very different, as discussed below. The fit to the experiment (dark solid lines) and the components of the fit (light solid lines) are shown in Figure 3. The best-fit parameters are given in the Supporting Information.

Experimental spectra show pronounced variations in the intensity ratios of the Pb 4f signal appearing between 135 and 145 eV and the P 2p signal between 130 and 135 eV upon changing the photon energy and also upon changing the size of the nanocrystals. Even without a quantitative analysis, the spectra provide some qualitative information concerning the structure of the nanocrystals. For example, if we focus on the changes in the Pb-to-P intensity ratio with changing photon energies for a given sample, it is readily seen that the overall relative intensity of the P 2p signal increases rapidly with decreasing photon energy, establishing that all phosphorus signals arise from an outer or surface layer compared to the Pb signals. Additionally, we find that the smallest nanocrystal sample has the largest P/Pb intensity ratio, followed by the intermediate sized nanocrystal sample at any given photon energy. The largest NCs have the lowest relative P content. This suggests that the smallest nanocrystals have the largest relative surface area, since P, as a part of the capping agent, is only on the surface of the nanocrystals. This is indeed to be expected since the surface-to-volume ratio decreases monotonically with increasing size of the nanocrystal.

To understand the origin of the two distinct P signals with peaks at 130 and 132.8 eV, we first note that a change in the binding energy of a core level of any elemental component in a compound compared to that in its elemental state, known as the chemical shift, depends on the charge state of that particular element in that compound; generally, one finds an increasing[25] binding energy with an increasingly positive charge state, primarily because of changes in the electronic repulsion. Keeping this in mind, we can assign the P species with a P 2p core level appearing at the lower binding energy of 130 eV to free TOP that does not bind to the nanocrystals. The other P 2p feature present at the higher binding energy of 132.8 eV is due to TOPSe that caps the surface of the nanocrystals. In an earlier work on CdSe NCs,[18] the P 2p feature with the lower binding energy was assigned to TOP bound to Cd atoms on the surface of the nanocrystals, and the feature with the higher binding energy was assigned to trioctylphosphine oxide (TOPO) bonded to the nanocrystals. However, we clearly find that the 130 eV P 2p component is even more surface sensitive compared to the TOPSe component at 132.8 eV, as evident from the strong relative enhancement of the signal at 130 eV with decreasing photon energy in the case of every sample (Figure 3), and thus the signal at 130 eV must be from the outermost layer. This suggests that some amount of TOP lies on the surface of the TOPSe layer, which is bonded to the nanocrystal surface.

Next we consider the details of the Pb 4f spectral features in Figure 3. The Pb 4f feature from all the samples could not be described in terms of a single Pb species with a 4f core-level split by spin−orbit interaction with a splitting of 4.8 eV; it requires at least two Pb species, as already discussed. These two components are shown with thin lines in Figure 3. We attribute the component at the higher binding energy to Pb present near the core of the nanocrystal, since its intensity increases as the photon energy is increased to probe more of the core material compared to the surface, as evident from Figure 3. The component at the lower binding energy is therefore due to the presence of Pb closer to the surface of the nanocrystal. In the case of PbS NCs,[19] the Pb species from the core of the NCs has been assigned a lower binding energy compared to that of the surface Pb. In that case, the surface Pb has been assigned to Pb bonded to the capping agent, oleic acid, since Pb−S has a lower binding energy compared to that of Pb−O.[26] In the samples studied here, we find the reverse trend, and thus surface Pb cannot be ascribed to Pb bonded to oleic acid, since the binding energy of Pb−Se is lower than the binding energy of Pb−O.[27] These results provide us with a model of a nanocrystal that has an outermost layer of adsorbed TOP, a surface layer of TOPSe ligands, and a core consisting of PbSe with a near-surface layer that has Pb^{2+} ions and Se ions in some form, distinct from the PbSe in the core of the NC. We shall now discuss the nature of the Se species in the next section.

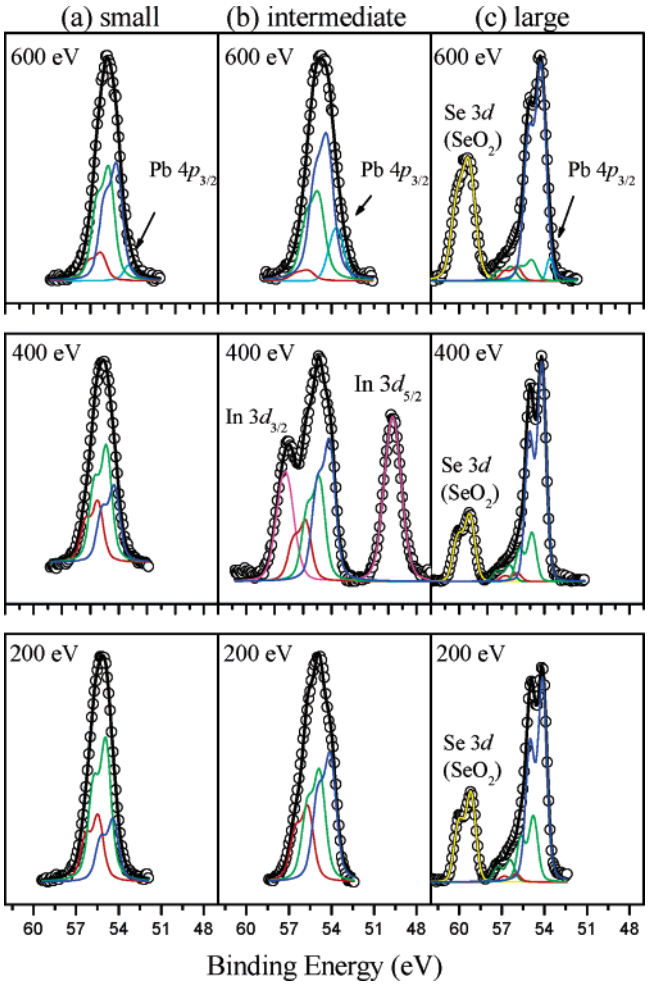

Figure 4. Background-subtracted Se 3d photoemission spectra and fits of (a) small, (b) intermediate, and (c) large PbSe nanocrystals.

Se 3d Spectra. The binding energy of the 3d core level in elemental Se is reported[28] at 54.6 eV with a $3d_{5/2}$ and $3d_{3/2}$ spin−orbit splitting of 0.9 eV. To study the relative surface-to-bulk sensitivity of the Se 3d feature, photoemission spectra were recorded at 600, 400, and 200 eV photon energies, as shown in Figure 4 for the small (4a), intermediate (4b), and large (4c) nanocrystals. The open circles represent the experimental data points, and the solid lines show the results of our theoretical analysis. Before discussing the analysis of the spectral shape in detail, we note that there are evidently extra spectral features appearing only for the intermediate sized sample (Figure 4b) at 49.6 and 57.3 eV apparent binding energies when the spectrum is recorded with a photon energy of 400 eV (middle panel). These two features are easily interpreted as In $3d_{5/2}$ and $3d_{3/2}$ signals from the substrate In foil due to pinholes in the sample powder pressed on the foil in this particular case. The true binding energies of the In $3d_{5/2}$ and $3d_{3/2}$ levels are 451.4 and 443.9 eV, respectively, thus they are approximately 400 eV higher than the Se 3d binding energy. Since the photon energy selected by the monochromator setting at a synchrotron source

is invariably accompanied by some photon intensity with double the selected photon energy due to the second-order diffraction effects, the 400 eV photon energy is invariably mixed with a certain portion of $h\nu = 800$ eV radiation. These 800 eV photons make the In 3d signal appear in the same spectral range as that of Se 3d excited with $h\nu = 400$ eV. A similar effect also occurs for the $h\nu = 600$ eV case, shown in the upper panels of Figure 4a−c, though in a less evident manner. The second-order $h\nu = 1200$ eV photons make the Pb $4p_{3/2}$ signal, with a true binding energy of 643.5 eV,[29] appear in the same spectral range as the Se 3d signals at a binding energy of 53.6 eV excited with $h\nu = 600$ eV. The main effect of the overlapping Pb $4p_{3/2}$ signal, although weak, is to distort the lower binding energy side of the Se 3d signal in the top panels. Since this overlapping feature is inevitably present in any synchrotron work, it has to be explicitly taken into account when quantitatively analyzing the Se 3d signal in terms of different compounds and contributions.

Focusing on the spectral contributions only from Se species in the samples, an intense feature between 58 and 61 eV binding energy can only be discerned for the largest sample (Figure 4c), while all other samples, including the largest one, show the main Se 3d signal in the range of 52−58 eV binding energy. The high binding energy of the extra feature in the large sample corresponds to that of Se in SeO_2. Thus, we infer that, in the large nanocrystals, the surface capping is sparse, and some surface Se gets oxidized to form SeO_2. These SeO_2 molecules get separated from the nanocrystals and form separate clusters. These separated SeO_2 clusters could have also formed from the oxidation of some free (unbonded) TOPSe in this particular case. However, since SeO_2 appears separated from PbSe, evidenced from the invariance of its intensity relative to the intensity of the PbSe-related signal with changing photon energy, the exact origin of SeO_2 in this particular case is irrelevant, and its presence does not interfere in the data analysis to determine the internal structure of PbSe NCs. The spectral feature from SeO_2 could be easily fitted with a doublet, representing the spin−orbit split, two peaks due to Se $3d_{5/2}$ and $3d_{3/2}$ core-hole states separated by a spin−orbit splitting of 0.9 eV, and an intensity ratio of 6:4 according to the degeneracies. This single doublet feature is more evident at the lower photon energy of 200 eV because of an increase in overall spectral resolution. However, it is clear that the main Se 3d spectral feature in all the samples, appearing between 52 and 58 eV, cannot be described in terms of a single Se species with a simple doublet feature, for example, as in Figure 4b. To analyze the spectral features in terms of separate contributions from distinct Se species, we adopt the same approach as that used in the case of Pb 4f spectra, to find out the least number of such contributions able to describe the experimental data in terms of a least-squared-error process. This approach showed that the Se 3d spectral features could be described well with a minimum of three independent Se components for the smallest and intermediate sized NCs, as shown in terms of the thin lines representing the three components as well as the comparison of the simulated (thick line) and the experimental (open circles) spectra in Figure 4a,b. However, we found that the Se 3d spectral features from the largest NCs (Figure 4c), besides the three Se components in common with the other two samples, also required an extra (fourth) component appearing with the highest binding energy for a suitable description of the total spectra. The relative binding energies of these four components in conjunction with the photon energy dependence of their relative intensities allow us to understand both the chemical species responsible for each of these components and their location in the sample defining the internal structure of the nanocrystals. For example, the component at the lowest binding energy (∼54.5 eV for $3d_{5/2}$) must correspond to the most negatively charged species; therefore, we assign it to Se^{2-} ions present in the nanocrystals. The intensity of this component noticeably decreases with a decrease in the photon energy that increases the surface sensitivity of the photoemission process; this clearly establishes that the 54.5 eV component arises from the Se^{2-} ions at the innermost core region of the nanocrystals. In a similar manner, we attribute the feature with its $3d_{5/2}$ peak at ∼55 eV to diselenide bonds present near the surface of the nanocrystal, in view of its agreement with the reported binding energy of diselenides in the literature[30] and its intensity dependence on the photon energy. The third component, with its $3d_{5/2}$ peaks at about 55.5 eV binding energy, is assigned to the outermost Se component attached to the capping agent TOPSe on the surface of the nanocrystals. The fourth Se component, with $3d_{5/2}$ peak at ∼57 eV and appearing only for the largest nanocrystals (Figure 4c), has a binding energy higher than that of the other three components with Se ions in various degrees of a negatively charged state, but substantially less than that of Se^{4+} species in SeO_2. In view of this, we ascribe this component of Se to natural or free Se, which is an intermediate during the formation of SeO_2. Thus, this Se species is also, most likely, not attached to the nanocrystals and is thus not included in the analysis to deduce the internal structure of the NCs; this is further supported by the absence of this fourth Se species in the other two samples.

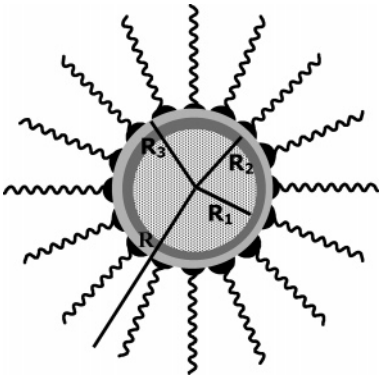

Figure 5. Schematic of the nanocrystal showing the different layers. R_1 is the radius of the PbSe core, $R_2 - R_1$ is the thickness of the $Pb_{1-x}Se$ shell, and $R_3 - R_2$ is the thickness of the surface Se layer. The effective thickness of the organic capping layer, t, is shown by the long chain.

Combining the results of the Pb 4f, P 2p, and Se 3d spectra, we arrive at the following model of the nanocrystals. The core of the nanocrystals consists of Pb^{2+} and Se^{2-} ions coordinated in the same manner as in bulk PbSe. The shell surrounding the core is made up of Pb^{2+} ions bound to Se^{2-} and diselenide ions. Thus, the composition of this layer is $Pb_{1-x}Se$. The next layer is purely Se ions that are attached to the capping layer. And finally, on the surface of the nanocrystals, chains of TOP are attached that passivate the surface. This is shown as a schematic in Figure 5. In the next subsection we use this model to determine the thickness of the various layers from a quantitative analysis of the spectral intensity and their variations with the photon energy.

Discussion

Figure 5 shows the schematic of a PbSe nanocrystal that we discussed in the last subsection. There are three layers of the nanocrystal shown in the figure and a fourth capping layer arising from TOP with an effective thickness, $R - R_3$. The radius

TABLE 1: Sizes of Different Layers (in nm) from the Analysis of the Photoemission Intensities[a]

	small	intermediate	large
cap thickness, $R - R_3$	1.2	1.0	1.0
nanocrystal radius, R_3	1.7 (3.4)	4.2 (8.4)	5.6 (11.2)
radius including the nonstoichiometric layer, R_2	1.3 (2.6)	4.1 (8.2)	5.5 (11.1)
PbSe core radius, R_1	1.1 (2.2)	3.6 (7.1)	5.0 (9.9)

[a] The corresponding diameters of the shells are given in parentheses.

of the core is given by R_1, the thickness of the $Pb_{1-x}Se$ shell is $R_2 - R_1$, and $R_3 - R_2$ is the effective thickness of the surface Se layer from TOPSe. Since the nanocrystals are essentially spherically symmetric, it is convenient to work in the spherical polar coordinates.[15,17] The total intensity I integrated over all the volume elements is given by

$$I = I_0 \int_{R'}^{R''} \int_0^{\pi} \int_0^{2\pi} \exp\left(-\frac{f(r,\theta)}{\lambda}\right) r^2 \mathrm{d}r \sin\theta \, \mathrm{d}\theta \, \mathrm{d}\varphi \quad (1)$$

where $f(r,\theta) = (R^2 - r^2 \sin^2\theta)^{1/2} - r\cos\theta$, and the r integration is carried out over the appropriate limits. Integration over φ is trivial because of the spherical symmetry involved; it gives a factor of 2π in each case, which can be eliminated if we use intensity ratios. The intensity ratio of the core to the other layers can be expressed by the following equations:

$$\frac{I_{Pb_{1-x}Se}}{I_{core}} = \frac{I_0^{Pb_{1-x}Se} \int_{R_1}^{R_2} \int_0^{\pi} \exp\left(-\frac{f(r,\theta)}{\lambda}\right) r^2 \mathrm{d}r \sin\theta \mathrm{d}\theta}{I_0^{PbSe} \int_0^{R_1} \int_0^{\pi} \exp\left(-\frac{f(r,\theta)}{\lambda}\right) r^2 \mathrm{d}r \sin\theta \, \mathrm{d}\theta} \quad (2)$$

$$\frac{I_{Se,surf}}{I_{core}} = \frac{I_0^{Se,surf} \int_{R_2}^{R_3} \int_0^{\pi} \exp\left(-\frac{f(r,\theta)}{\lambda}\right) r^2 \mathrm{d}r \sin\theta \, \mathrm{d}\theta}{I_0^{PbSe} \int_0^{R_1} \int_0^{\pi} \exp\left(-\frac{f(r,\theta)}{\lambda}\right) r^2 \mathrm{d}r \sin\theta \, \mathrm{d}\theta} \quad (3)$$

We need to determine the different I_0 values to obtain the ratios. The value of I_0 depends on the number density of the atoms that contribute to the photoemission signal. The number density is conveniently given by the ratio of the density, ρ, of the material to its molar mass, M. The only unknown is the value of x in the expression $Pb_{1-x}Se$, which is varied to get the best description for the ratios. For the surface Se atoms, we vary the number density, which always converges to twice the density, as in PbSe in each case, indicating there are only Se atoms in this layer. The thickness of the capping agent, $R - R_3$, is expected to be close to the length of a TOP chain, ~1.1 nm, since $R - R_3$ represents the extra distance the electron has to travel to escape to the vacuum starting from various layers within the nanocrystals, where the photoemission from Se, Pb, and P occurs. However, we allow the variable R to vary, thereby allowing the possibility of the TOP chain being somewhat flexible or sticking to the surface at an angle other than 90°.

Now we vary the values of R, R_1, R_2, and R_3 along with the value of x to obtain the best description for the intensity ratios obtained from different photon energies and various core levels obtained in our experiment. The best-fit values are given in Table 1 for the three different sizes of nanocrystals. An interesting fact worth noting is the change in the thickness of the nonstoichiometric layer, $R_2 - R_1$, which is very small in the case of the smallest PbSe NCs. This is also reflected in the intensity ratios of the two Pb signals seen in Figure 3 and is likely due to the exclusion of defects for very small NCs. For all three samples, the cap thickness of the shell is almost the same. This corresponds closely to the length of an octyl chain in TOP (~1.1 nm). The radii (R_2) of the nanocrystals agree well with those determined from TEM and XRD analysis; however, it is important to note that TEM and XRD can provide only a single value for the size of nanocrystals. For example, XRD provides the size estimate for only the crystalline core region, while TEM probably provides an estimate of R_2, since the TOPSe layer may not provide enough contrast to have clear identification in a transmission electron micrograph. In contrast, to these techniques, the present approach provides detailed information on the internal structure of the nanocrystals.

Luminescence quantum efficiencies depend on a number of factors governed by structural and electronic features of the nanocrystals. For example, faceted growth, stacking faults, and structural defects all lead to changes in the luminescence quantum yields. Also responsible for such changes is the presence of trap states in the nanocrystals. In light of the results obtained from our photoemission data, we propose a possible explanation for the changes in the luminescence efficiency with particle size. The thickness of the $Pb_{1-x}Se$ shell ($R_2 - R_1$) is small for the smallest nanocrystals. Thus, it seems likely that the $Pb_{1-x}Se$ layer leads to the formation of defects that lead to fluorescence quenching in the larger nanocrystals. Additionally, the thickness of the TOPSe layer given by ($R_3 - R_2$) decreases as one increases the NC size; specifically ($R_3 - R_2$), representing an average thickness of the passive layer of 0.38, 0.1, and 0.07 nm for the small, intermediate, and large NCs, respectively. This observation suggests that, since the TOPSe layer acts as a passivating layer for the surface of the nanocrystals, a loss of TOPSe from the NC surface, as in the case of the largest sample, leads to a loss in the fluorescence quantum efficiency.

In conclusion, we have performed photoemission experiments on three different sizes of PbSe nanocrystals. Using variable energy synchrotron radiation to tune the surface sensitivity of the core-level photoelectron experiment to obtain layer/depth specific information from passivated PbSe nanocrystals, we reveal a rich internal structure of these nanocrystals. We clearly identify at least two distinct species of Pb, three distinct species of Se, and two distinct species of P inherent to the nanocrystal. This contrasts the normal expectation of a single PbSe species capped with a single passivating agent and illustrates the complex microscopic structure adopted in reality by such nanocrystals. A careful analysis of the intensity variation of different core-level signals with photon energy provides us with detailed and quantitative information on the microscopic structure of these nanocrystals; we note that this is a unique strength of the present approach, as such information would be impossible to obtain from any other technique. These experiments also provide a plausible explanation for why the luminescence quantum yield decreases with an increase in the size of the Se nanocrystals.

Acknowledgment. This research is supported by the Department of Science and Technology, Government of India. The authors are thankful to ICTP, Trieste, Italy, for supporting the access to the Elettra synchrotron center, Trieste. We would also like to thank the scientific staff at the VUV beamline at Elettra. The LANL team thanks Victor Klimov for support and encouragement and Donald Werder for TEM measurements.

Supporting Information Available: Pb 4f/P 2p and Se 3d photoemission spectra for all three sizes of nanocrystals, along with their respective fit parameters. This material is available free of charge via the Internet at http://pubs.acs.org.

References and Notes

(1) Peng, X. G.; Schlamp M. C.; Kadavanich, A. V.; Alivisatos, A. P. *J. Am. Chem. Soc.* **1997**, *119*, 7019.

(2) Murray, C. B.; Sun, S.; Gaschler, W.; Doyle, H.; Betley, T. A.; Kagan, C. R. *IBM J. Res. Dev.* **2001**, *45*, 47.

(3) Gu, H.; Yang Z.; Gao, J.; Chang, C. K.; Xu, B. *J. Am. Chem. Soc.* **2005**, *127*, 34.

(4) Mokari T.; Rothenberg, E.; Popov, I.; Costi, R.; Banin, U. *Science* **2004**, *304*, 1787.

(5) Wong, E. M.; Hoertz P. G.; Liang, C. J.; Shi, B.; Meyer, G. J.; Searson, P. C. *Langmuir* **2001**, *17*, 8362.

(6) Puzder, A.; Williamson, A. J.; Zaitseva, N.; Galli, G.; Manna, L.; Alivisatos, A. P. *Nano Lett.* **2004**, *4*, 2361.

(7) Bullen, C. R.; Mulvaney, P. *Nano Lett.* **2004**, *4*, 2303.

(8) Pesika, N. S.; Hu, Z.; Stebe, K. J.; Searson, P. C. *J. Phys. Chem. B.* **2002**, *106*, 6985.

(9) Talapin, D. V.; Poznyak, S. K.; Gaponik, N. P.; Rogach, A. L.; Eychmuller, A. *Physica E* **2002**, *14*, 237. Talapin, D. V.; Rogach, A. L.; Mekis, I.; Haubold, S.; Kornowski, A.; Haase, M.; Weller, H. *Colloids Surf., A* **2002**, *202*, 145.

(10) Jones, M.; Nedeljkovic, J.; Ellingson, R. J.; Nozik, A. J.; Rumbles, G. *J. Phys. Chem. B* **2003**, *107*, 11346. Wuister, S. F.; Houselt, A. V.; Mello Donega, C.; Vanmaekelbergh, D.; Meijerink, A. *Angew. Chem., Int. Ed.* **2004**, *43*, 3029.

(11) Tsay, J. M.; Doose, S.; Pinaud, F.; Weiss, S. *J. Phys. Chem. B* **2005**, *109*, 1669.

(12) Sachleben, J. R.; Colvin, V.; Emsley, L.; Wooten, E. W.; Alivisatos, A. P. *J. Phys. Chem. B* **1998**, *102*, 10117. Tomaselli, M.; Yarger, J. L.; Bruchez, M.; Havlin, R. H.; deGraw, D.; Pines, A.; Alivisatos, A. P. *J. Chem. Phys.* **1999**, *110*, 8861.

(13) Ladizhansky, V.; Hodes. G.; Vega, S. *J. Phys. Chem. B* **1998**, *102*, 8505. Berrettini, M. G.; Braun, G.; Hu, J. G.; Strouse, G. F. *J. Am. Chem. Soc.* **2004**, *126*, 7063.

(14) Hamad, K. S.; Roth, R.; Rockenberger, J.; van Buuren, T.; Alivisatos, A. P. *Phys. Rev. Lett.* **1999**, *83*, 3474. Rajh, T.; Chen, X. L.; Lukas, K.; Liu, T.; Thurnauer, M. C.; Tiede, D. M. *J. Phys. Chem. B* **2002**, *106*, 10543.

(15) Nanda, J.; Kuruvilla, B. A.; Sarma, D. D. *Phys. Rev. B* **1999**, *59*, 7473.

(16) Winkler, U.; Eich, D.; Chen, Z. H.; Fink, R.; Kulkarni, S. K.; Umbach, E. *Chem. Phys. Lett.* **1999**, *306*, 95.

(17) Nanda, J.; Sarma, D. D. *J. Appl. Phys.* **2001**, *90*, 2504.

(18) Borchert, H.; Talapin, D. V.; McGinley, C.; Adam, S.; Lobo, A.; de Castro, A. R. B.; Möller, T.; Weller, H. *J. Chem. Phys.* **2003**, *119*, 1800. Nowak, C.; Dollefeld, H.; Eychmuller, A.; Friedrich, J.; Kolmakov, A.; Lofken, J. O.; Riedler, M.; Wark, A.; Weller, H.; Wolff, M.; Moller, T. *J. Chem. Phys.* **2001**, *114*, 489. Dollefeld, H.; McGinley, C.; Almousalami, S.; Moller, T.; Weller, H.; Eychmuller, A. *J. Chem. Phys.* **2002**, *117*, 8953.

(19) Lobo, A.; Möller, T.; Nagel, M.; Borchert, H.; Hickey, S. G.; Weller, H. *J. Phys. Chem. B* **2005**, *109*, 17422.

(20) Felix, C.; Bewley, W. W.; Vurgaftman, I.; Lindle, J. R.; Meyer, J. R.; Wu, H. Z.; Xu, G.; Khosravrani, S.; Shi, Z. *Appl. Phys. Lett.* **2001**, *78*, 3770.

(21) Wehrenberg, B. L.; Wang, C.; Guyot-Sionnest, P. *J. Phys. Chem. B* **2002**, *106*, 10634.

(22) Pietryga, J. M.; Schaller, R. D.; Werder, D.; Stewart, M. H.; Klimov, V. I.; Hollingsworth, J. A. *J. Am. Chem. Soc.* **2004**, *168*, 11572.

(23) Schaller, R. D.; Petruska, M. A.; Klimov, V. I. *J. Phys. Chem. B* **2003**, *107*, 13765.

(24) Nanda, J.; Sapra, S.; Sarma, D. D. *Encyclopedia of Nanoscience and Nanotechnology*; Nalwa, H. S., Ed.; American Scientific Publishers: Los Angeles, CA, 2004; Vol. 10, p 711.

(25) Rao, C. N. R.; Sarma, D. D.; Hegde, M. S. *Proc. R. Soc. London* **1979**, *A367*, 239.

(26) Laajalehto, K.; Smart, R. St. C.; Ralston, J.; Suoninen, E. *Appl. Surf. Sci.* **1993**, *64*, 29.

(27) NIST Database. http://srdata.nist.gov/xps (accessed Dec 2005).

(28) Cardona, M.; Ley, L. *Photoemission in Solids*; Springer-Verlag: New York, 1978; Vol. 1.

(29) Yeh, J. J.; Lindau, I. *At. Data Nucl. Data Tables* **1985**, *32*, 1.

(30) Krishnakumar, S. R.; Sarma, D. D. *Phys. Rev. B* **2003**, *68*, 155110.